

Surface modification of hierarchical hydroxyapatite fabricated via hydrothermal method



Fatemeh Mohandes ^{a,b,*}, Elvira Gómez ^{a,b}, Albert Serrà ^{a,b}

^a Grup d'Electrodepositió de Capes Primes i Nanoestructures (GE-CPN), Departament de Ciència de Materials i Química Física, Universitat de Barcelona, Martí i Franquès, 1, E-08028, Barcelona, Catalonia, Spain

^b Institute of Nanoscience and Nanotechnology (IN2UB), Universitat de Barcelona, Barcelona, Catalonia, Spain

ARTICLE INFO

Handling Editor: Dr P. Vincenzini

Keywords:

Biomaterials
Functionalization
Hydroxyapatite
Bisphosphonate
Hierarchical

ABSTRACT

Surface modification, encompassing both chemical and physical features, plays a crucial role in fulfilling the requirements of biomaterial applications and also improves their performance. Due to that, this study focuses on the optimization of morphology and functionalization of hydroxyapatite (HAP). For this purpose, hydrothermal growth of HAP on (fluorine tin oxide) FTO is carried out in the presence of calcium and phosphate precursors with Ca/P molar ratio of 1.67:1 in the solution. Trisodium nitrilotriacetic acid (NTA) is used as a chelating additive for the first time during hydrothermal process at temperature between 120 and 180 °C for 16–24 h. Further studies on the effect of NTA concentration on HAP formation indicate that hierarchical structures are formed in the presence of NTA with NTA/Ca molar ratio of 1:1 at temperature between 150 and 180 °C for 24 h, improving crystallinity as temperature increasing. To facilitate the functionalization of HAP, the layer deposited at 180 °C with NTA/Ca molar ratio of 1:1 is peeled using two different reagents, Fluoromount™ and polyvinyl alcohol (PVA). The HAP peeled with PVA shows no relevant morphological changes in SEM images, indicating a successful peeling process using PVA. After that, the HAP powders are functionalized with alendronate (AL) molecules and studied using ATR-FTIR, XPS and BET techniques. Chemical shift of PO_4^{3-} vibrations and appearance of the new peaks assigned to the $-\text{NH}_2$ group demonstrate successful AL-functionalization. The AL-HAP hierarchical structures fabricated with the aid of NTA can be introduced as multifunctional biomaterials for future bio-applications.

1. Introduction

Design, fabrication and modification of biomaterials in both morphological and composition features to treat, replace, or detect damaged tissues and organs in the body have garnered significant interest among researchers. This interest is attributed to their biocompatibility in response to cells and biodegradation in the physiological environment [1–4]. The first generation of biomaterials, consisting of methacrylate polymers, only provided physical properties resembling replaced tissue without establishing biological interactions with the surrounding tissue. To overcome this problem, the second generation, termed “bioactive” materials with biological interactions, was introduced [1]. By combining the bioactivity and biodegradation properties as well as having biological signals, the third and fourth generations of biomaterials were sequentially disclosed, which are able to regenerate

damaged tissues [1,2].

Among the wide range of recommended biomaterials, hydroxyapatite (HAP; $\text{Ca}_{10}(\text{PO}_4)_6(\text{OH})_2$) as a member of calcium phosphate (CP) family [5] has attracted significant attention due to its excellent biocompatibility, bioactivity, and ability to form chemical bonds with living tissues [6,7]. Compared to the other calcium phosphates, HAP is the top stable member in biological media without producing cytotoxic by-products [8]. Consequently, extensive research is ongoing to prepare HAP with desired chemical and physical properties. Various techniques to fabricate HAP, such as sol-gel [9], precipitation [10], hydrothermal [11,12] and biomimetic deposition on collagen membrane [13], have been developed. While wet methods require control over morphology and particle size, the low temperature of the processes can lead to the formation of low-crystalline HAP [14].

Compared to the sol-gel and precipitation routes, hydrothermal

* Corresponding author. Grup d'Electrodepositió de Capes Primes i Nanoestructures (GE-CPN), Departament de Ciència de Materials i Química Física, Universitat de Barcelona, Martí i Franquès, 1, E-08028, Barcelona, Catalonia, Spain.

E-mail address: mohandes@ub.edu (F. Mohandes).

Table 1
Preparation conditions of HAP under hydrothermal process.

Sample	NTA:Ca molar ratio	Temperature (°C)	Time (h)	Morphology (<i>via</i> SEM imaging)
S1	1:1	120	24	Irregular plate-like shapes
S2	1:1	150	24	Hierarchical microparticles composed of needle-like nanorods
S3	1:1	165	24	Aggregated nanorods
S4	1:1	180	24	Hierarchical flower-like microparticles
S5	0:1	180	24	Irregular micro/nanorods needle-like nanorods
S6	0.5:1	180	24	Needle-like nanorods
S7	2:1	180	24	Aggregated nanorods
S8	4:1	180	24	Aggregated nanorods

Total volume of the solutions and Ca/P molar ratio are 10 mL and 1.67:1, respectively, in the all experiments.

process, owing to its high temperature and pressure, can improve the crystallinity of HAP [15]. In addition, crystal shape and dimensions can be easily controlled by additives, as well as optimized temperature and time during hydrothermal synthesis. For instance, the synthesis of hierarchical structures composed of rod-like shapes, with the aid of disodium ethylenediaminetetraacetic acid (EDTA), has revealed that organic additives, including carboxylate and amine groups, can coordinate with Ca^{2+} ions to form chelate complexes, providing precursor for nucleation process. The hydrocarbon chains of the additives might control the orientation of crystal growth during hydrothermal conditions [16–18]. Recent studies have also focused on sodium citrate-assisted hydrothermal synthesis of HAP with hierarchical morphology because of their three-dimensional (3-D) structure and porosity [19–21].

In addition to the aforementioned chelating agents, trisodium nitrotriacetic acid (NTA), which includes three carboxylate groups bonded to a central nitrogen atom, has been found as a tetradeinate chelating agent [22]. Although NTA has been used as additive to produce

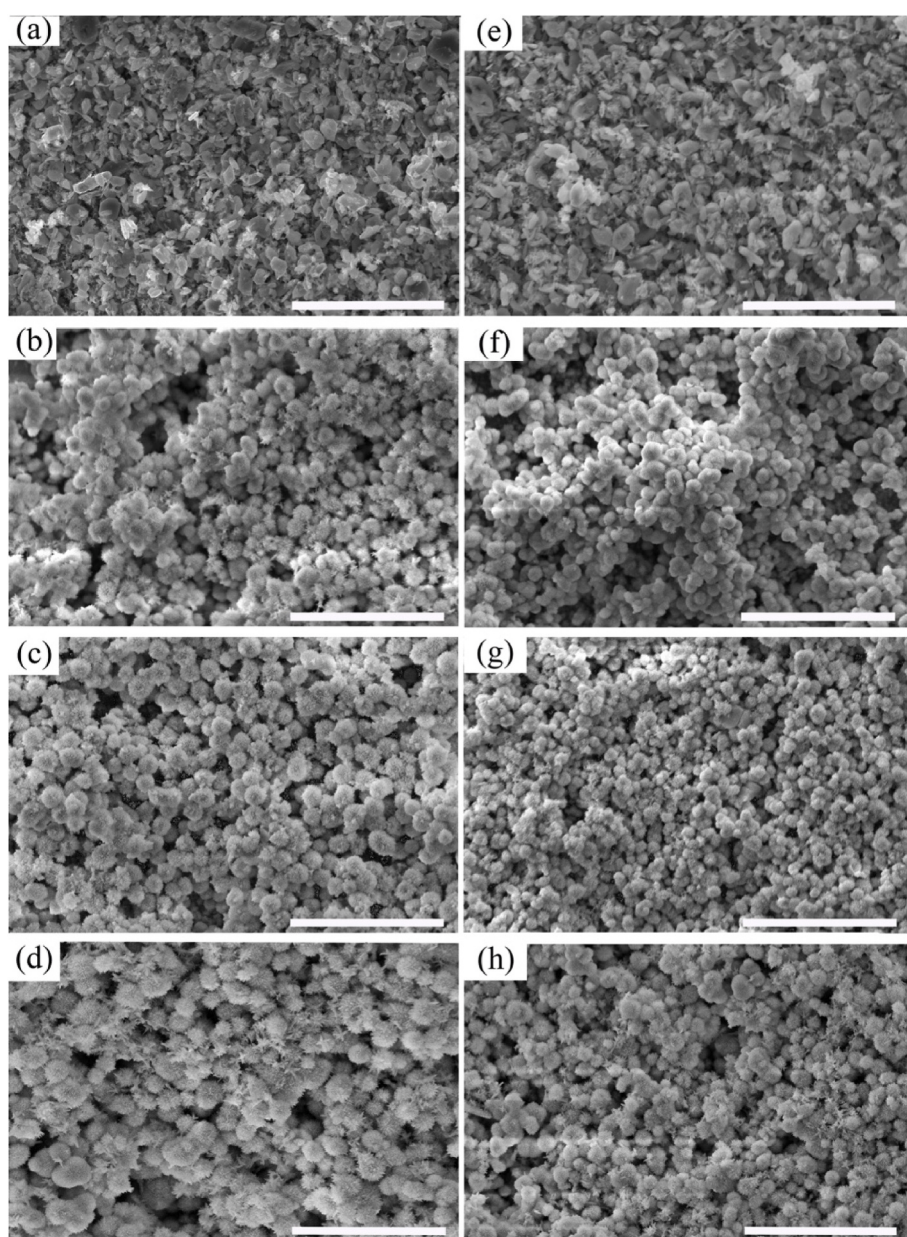


Fig. 1. SEM images of the as-prepared HAP at various hydrothermal temperatures: 120 °C (a), 150 °C (b), 165 °C (c), and 180 °C (d), and the corresponding samples after thermal treatment at 400 °C for 30 min (e–h). Molar ratios of NTA/Ca and Ca/P are 1:1 and 1.67:1, respectively. Scale bar is 50 μm .

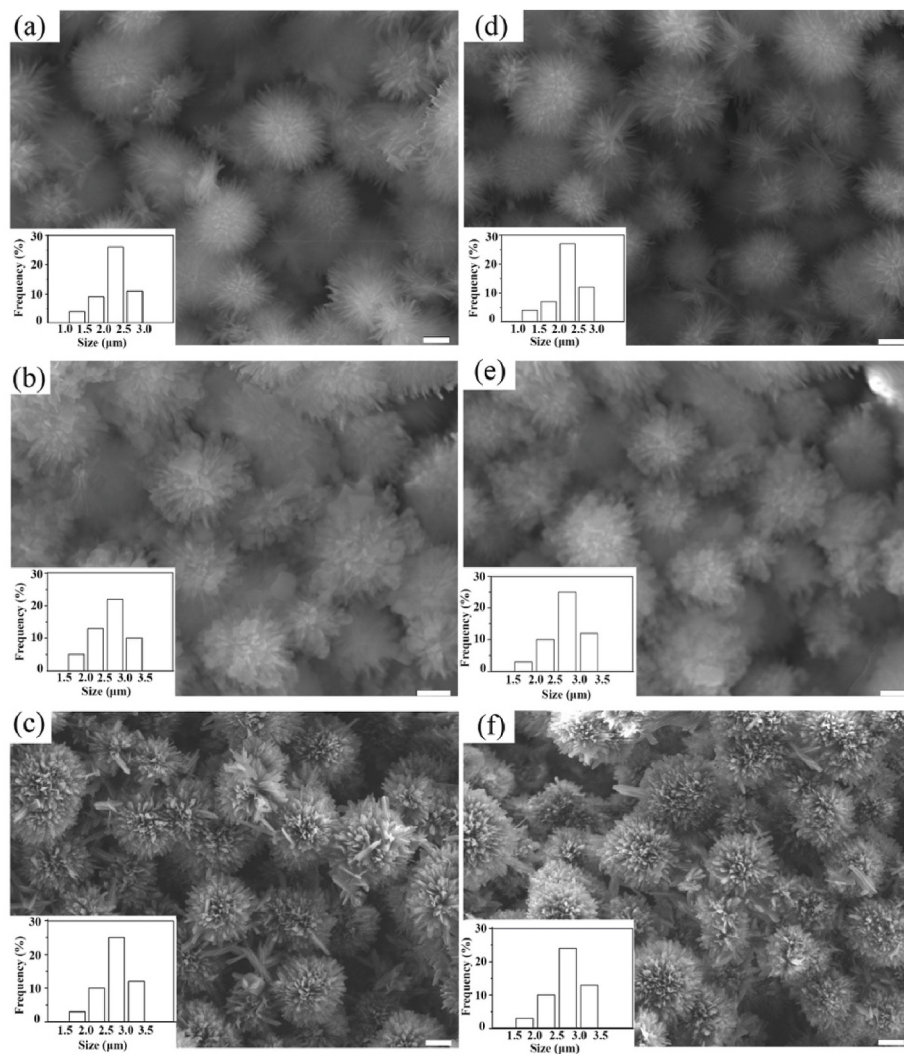


Fig. 2. FE-SEM images of hierarchical HAP prepared at various hydrothermal temperatures: 150 °C (a), 165 °C (b), and 180 °C (c), and the corresponding samples after thermal treatment at 400 °C for 30 min (d–f). Molar ratios of NTA/Ca and Ca/P are 1:1 and 1.67:1, respectively. The insets show particle size distribution. Scale bar is 1 μm.

Table 2

Estimated sizes of the hierarchical HAP particles using FE-SEM images and Fiji software.

Sample	Mean size (μm)	Standard deviation (SD)	Min (μm)	Max (μm)
S2	2.2	0.4	1.5	2.7
S2T	2.3	0.3	1.6	2.9
S3	2.7	0.4	2.0	3.2
S3T	2.8	0.3	2.2	3.3
S4	2.8	0.5	2.5	3.4
S4T	2.8	0.4	2.6	3.7

hierarchical structures of metal compounds via hydrothermal method [23–25], there is no investigation into the effect of NTA on the preparation of HAP. Since NTA selectively coordinates to Ca^{2+} ions to form $[\text{Ca}(\text{NTA})]$ complex, even in the presence of Na^+ , K^+ or Mg^{2+} ions [26], revealing the potential effect of NTA on crystal growth of HAP.

To date, although the demand for biomaterials is increasing, the biological response remains the main scientist's concern. To overcome this challenge, the surface properties of biomaterial should be modified, as the surface is the first region that comes into contact with the physiological environment [27]. It is anticipated that functionalization of biomaterials can develop their chemical and physical properties to

establish efficient interface with biomolecule [28–31].

Currently, much attention is focused on amino-bisphosphonates as multifunctional reagents, owing to their low toxicity and biocompatibility [32–35]. Amino-bisphosphonates, such as pamidronate (PAM), alendronate (AL) and zoledronate (ZOL), exhibit greater bonding affinity to calcium minerals compared to the non-amino-bisphosphonates due to their electrostatic interactions and hydrogen bonding [36,37]. AL molecule, in particular, has a central carbon atom attached to hydroxyl, phosphates, and NH_2 -terminated $(-\text{CH}_2)_3$ chain, improving surface interactions via the side groups [38]. Both experimental and computational studies have confirmed the satisfactory binding affinity of AL with HAP [39], introducing the multifunctional AL-HAP compound [40]. To address this issue, the conjugation of the side groups of AL with fluorophores [35] and chemo-photothermal agents [41] displays multifunctional behavior of HAP functionalized by AL.

In this study, HAP was hydrothermally deposited on substrate in the presence of calcium and phosphate precursors. For the first time, NTA was used as an organic additive to promote the fabrication of hierarchical HAP microparticles. The effect of preparation parameters on the HAP morphology and its crystalline phase was investigated using scanning electron microscopy (SEM) and X-ray powder diffraction (XRD). To functionalize HAP, the as-deposited layer was peeled with the aid of water-soluble polymers to obtain HAP powders. After the peeling

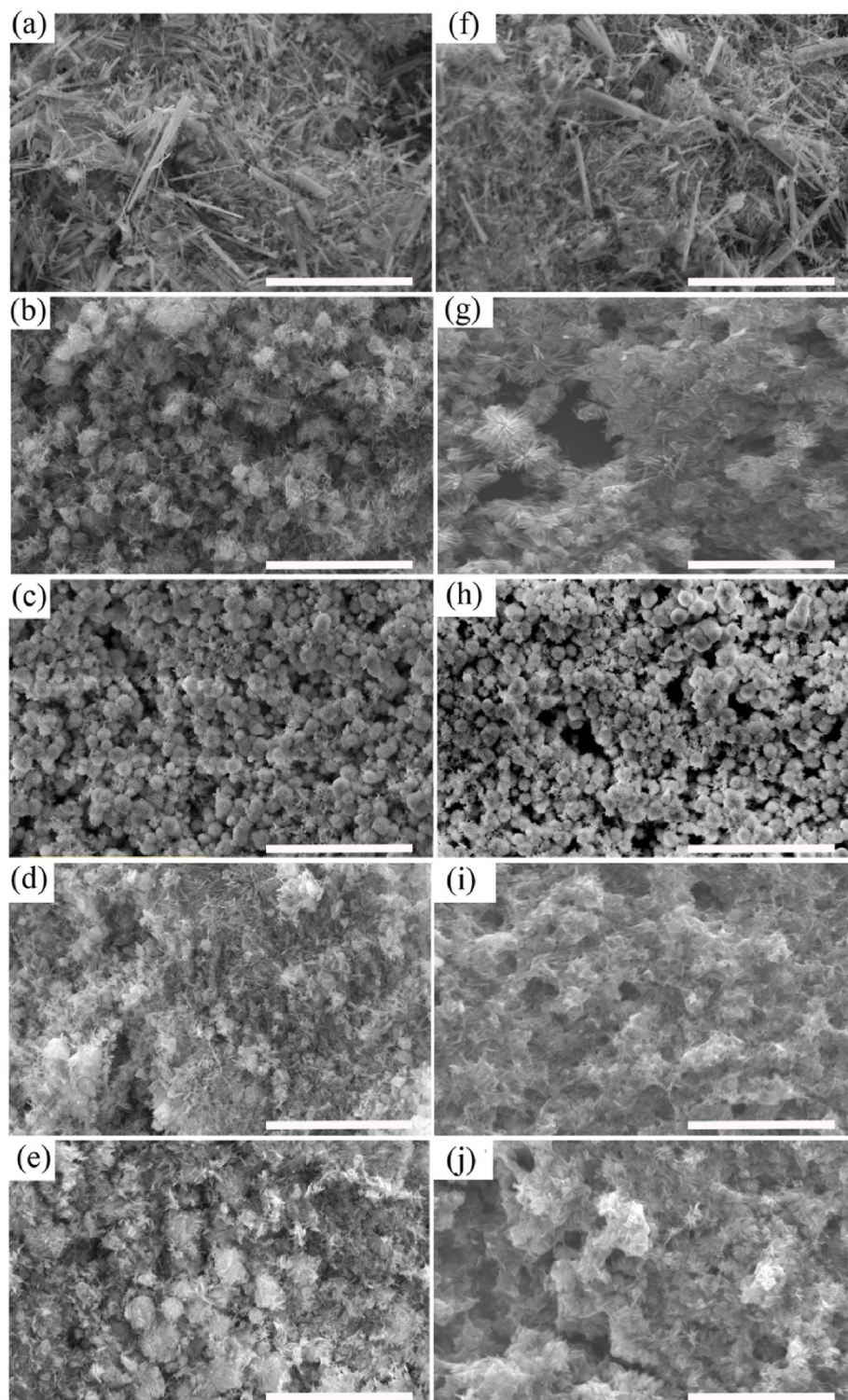


Fig. 3. SEM images of the as-prepared HAP at 180 °C for 24 h with various NTA/Ca molar ratios: 0:1 (a), 0.5:1 (b), 1:1 (c), 2:1 (d), and 4:1 (e), and the corresponding samples after thermal treatment at 400 °C for 30 min (f–j). Molar ratio of Ca/P is 1:1 for all the samples. Scale bar is 50 μm .

and purification process, HAP powders were treated with AL molecules for functionalization. To confirm the surface modification of HAP with AL molecules, Fourier transform infrared (FTIR) spectroscopy was used.

2. Materials and methods

2.1. Chemicals

Calcium chloride anhydrous granules (CaCl_2 , Sigma-Aldrich), ammonium dihydrogen phosphate ($\text{NH}_4\text{H}_2\text{PO}_4$, analysis grade, Sigma-Aldrich), nitrilotriacetic acid trisodium salt monohydrate (NTA; 98.0%, Aldrich), polyvinyl alcohol (PVA; Merck, MW = 89,000–98,000

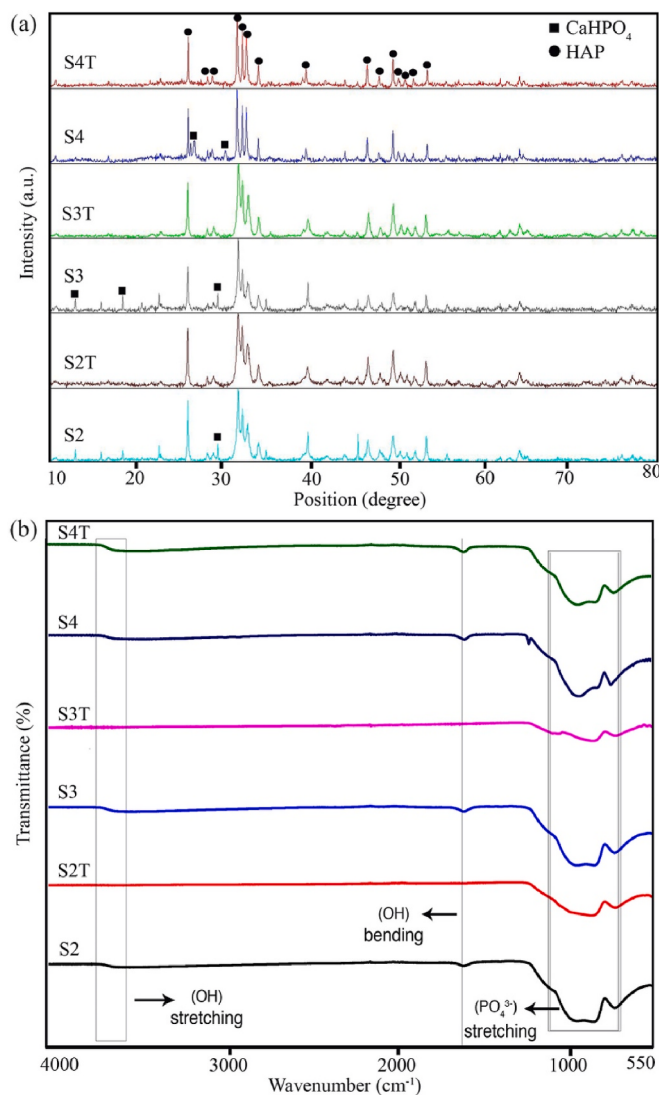


Fig. 4. (a) XRD patterns and (b) ATR spectra of the as-deposited HAP at 150 °C (S2), 165 °C (S3), 180 °C (S4), as well as the corresponding samples after thermal treatment at 400 °C for 30 min (S2T–S4T). Molar ratios of NTA/Ca and Ca/P of the samples are 1:1 and 1.67:1, respectively.

Da, 99% hydrolyzed), Fluoromount™ (Sigma-Aldrich), alendronate sodium (AL; PHR1599, Sigma-Aldrich), and ethanol (96%, Panreac) were used without purification. To prepare the solutions and wash the products, MilliQ treated water was used. Transparent FTO glass (Ref. FTO AGC80/1.1, Aldrich) was used as substrate.

2.2. Fabrication of HAP

The growth of HAP was carried out on FTO glass by hydrothermal method. First, the FTO substrate (1.0 cm^2) was cleaned ultrasonically with acetone, ethanol, and water separately for 2 min, placed upside down in a Teflon vessel (50 mL), and then autoclaved at temperature between 120 and 180 °C for 16–24 h in the presence of a solution consisted of CaCl_2 and $\text{NH}_4\text{H}_2\text{PO}_4$ precursors with and without NTA. Different quantities of NTA with molar ratios from 0 to 4 regard to CaCl_2 (NTA/Ca) was added into 5 mL of aqueous CaCl_2 solution (1.67 mM). When the solution was stirred for 30 min, 5 mL of aqueous $\text{NH}_4\text{H}_2\text{PO}_4$ solution (1.0 mM) was added dropwise into the Ca-NTA solution, stirred for 10 min, and then transferred to the autoclave. After cooling the autoclave naturally to room temperature, the as-prepared coated substrate was immersed in water (50 °C) for 2 min to remove the unreacted

reagents. This treatment was repeated five times. Finally, the samples were dried at 100 °C overnight, and heated at 400 °C for 30 min in air. The Ca/P molar ratio was constant in the all experiments (1.67:1). The preparation conditions have been summarized in Table 1.

2.3. Peeling of HAP layer

In order to peel the HAP formed on FTO glass, 10 μL of Fluoromount™ was drop casted on the surface, and then the glass was kept in desiccator to dry the film. After 2 days, the glass was stayed in Petri dish including 5 mL of water. At these conditions, polymer dissolved in water and HAP particles released. After collecting the particles at the bottom of the Petri dish, the excess polymer was removed by washing the powders several times with water and ethanol, and dried at 100 °C for 24 h. The same peeling conditions were repeated with 10 μL of PVA solution (80 mg/mL) instead of Fluoromount™.

2.4. Functionalization

A wet-chemical process has been applied for functionalization of the peeled HAP powders with AL molecules. In a typical procedure, 10 mL of aqueous AL solution (8 mM) was added into 10 mL of aqueous suspension (200 ppm) of HAP, stirred at room temperature for 24 h at 500 rpm, centrifuged, washed several times with water and ethanol, finally dried at 100 °C for 24 to characterize. The thermal-treated sample fabricated at 180 °C with NTA/Ca molar ration of 1:1 was selected for AL-functionalization.

2.5. Apparatus

To investigate the morphological changes of HAP prepared in various conditions, low-magnification and high-magnification images of carbon-coated samples were provided by Quanta 200 FEI, XTE 325/D8395 and FE-SEM, JEOL J-7100, respectively. Size distribution of the particles were also estimated by Fiji software using FE-SEM images for more than 50 particles. Formation of HAP was studied by attenuated total reflectance (ATR) of Fourier transform infrared (FTIR) spectroscopy (Nicolet iS5 with iD7 ATR, Thermo Scientific). In addition, crystalline phase of HAP was determined using X-ray single crystal diffractometer Bruker D8 Venture (Cu K α_1 radiation: $\lambda = 1.5406 \text{ \AA}$, work power of 45 kV and current of 40 mA). Surface composition of HAP before and after functionalization was analyzed by X-ray photoelectron spectroscopy (XPS) performed with an equipment based on the PHI 5000 VersaProbe instrument from Physical Electronics (ULVAC-PHI), monochromatic focused on X-ray source (Al K $\alpha = 1486.6 \text{ eV}$) calibrated using the 3d5/2 line of Ag with a full width at half maximum of 0.6 eV. The analyzed area of XPS was a circle of 100 μm in diameter, and all the measurements were made in an ultra-high vacuum (UHV) chamber at a pressure between 5×10^{-10} and 5×10^{-9} Torr. Specific surface area of the as-prepared HAP and functionalized HAP was studied using Brunauer-Emmett-Teller (BET) method (TriStar 3000, Micromeritics, USA). The measurements were conducted with solid samples (0.5 g) after N_2 degassing at 100 °C for overnight at P/P_0 values of 0.10, 0.125, 0.15, 0.20, 0.25. Thermal behavior of HAP after functionalization was considered and compared with the pure HAP by thermal gravimetric analysis (TGA) using a Thermobalance Mettler TGA/SDTA851e (Mettler Toledo AG, Switzerland) analyzer from room temperature to 800 °C at heating range of 10 °C/min under N_2 .

3. Results and discussion

Experimental variables of hydrothermal approach, such as temperature, time and reagent concentration, play a key role to control particle size and shape of HAP [42]. In this context, the influence of hydrothermal temperature and time on the HAP morphology is examined.

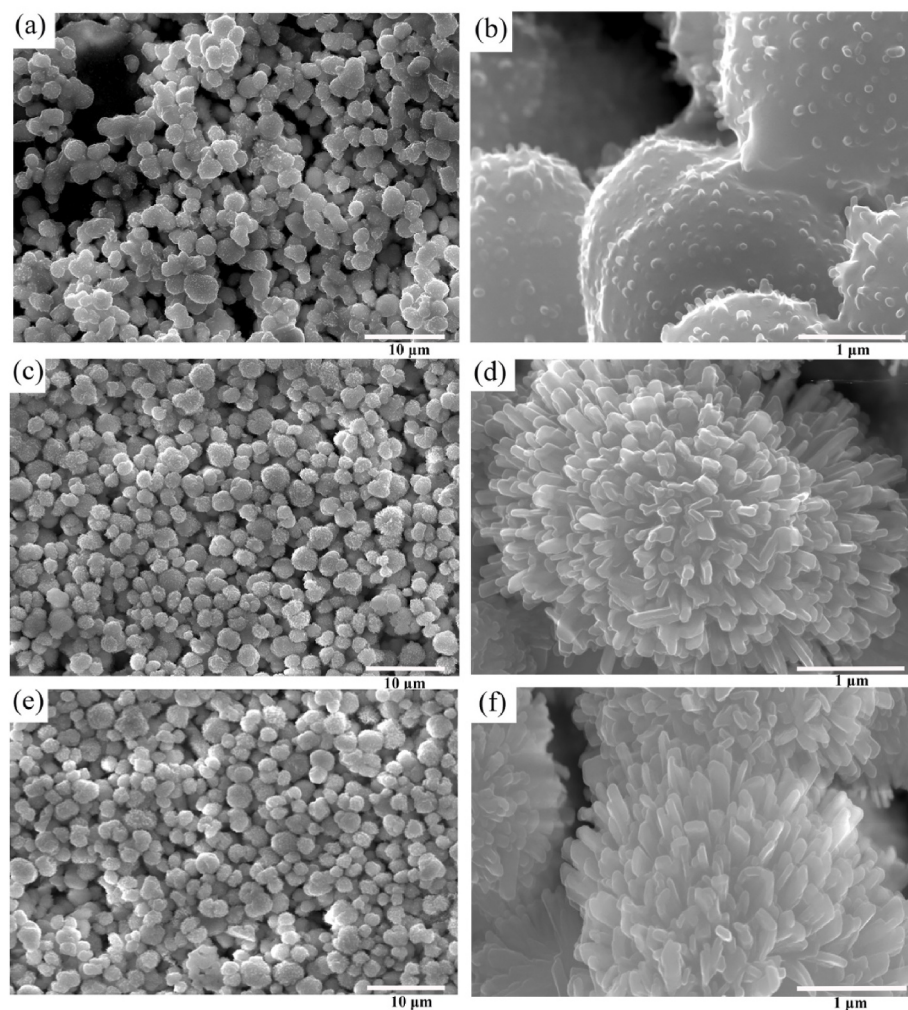


Fig. 5. Low-magnification and high-magnification FE-SEM images of the HAP layers fabricated at 180 °C with NTA/Ca molar ratio of 1:1 (S4T) after peeling with: (a, b) FluoromountTM, (c,d) PVA, and (e,f) PVA along with AL-functionalized.

SEM images of the as-deposited samples at different temperatures (S1–S4) and after thermal treatment (S1T–S4T) have been taken and presented in Fig. 1a–d and Fig. 1e–h, respectively. The molar ratios of NTA/Ca and Ca/P of the samples S1–S4 are 1:1 and 1.67:1, respectively.

Characterization of HAP precipitated at temperature below 100 °C shows low stability and crystallinity of the product [43,44]. To improve both of stability and crystallinity, HAP was precipitated during hydrothermal rout at temperature between 120 and 180 °C. When the hydrothermal process was carried out at 120 °C, almost all of the particles have plate-like structures with irregular shapes and inhomogeneous sizes. Upon increasing the temperature from 120 to 150 °C, some microparticles hierarchically form via self-assembly of needle-like rods. At this temperature, morphology composes of needle-like rods aggregated on the surface of the microparticles. As the reaction performed at 165 and 180 °C, uniform flower-like hierarchical microparticles could be obtained. It is clear that the dimensions of the particles fabricated at 180 °C are larger than those of the particles formed at 165 °C. It must be noted that the morphology of the as-fabricated HAP by hydrothermal rout has no change after thermal treatment at 400 °C for 30 min.

For a detailed morphological analysis, high-magnification FE-SEM images are provided in Fig. 2. The insets of Fig. 2 show particle size distribution of approximate 50 particles, analyzed using Fiji software. It should be noted that the increase of hydrothermal temperature leads to the increase of particle size. The estimated particle sizes of the HAP particles synthesized at 150, 165 and 180 °C summarized in Table 2 are 2.2 ± 0.4 , 2.7 ± 0.4 , and 2.8 ± 0.5 μm, respectively. By comparing the

SEM images of the HAP fabricated at various temperatures, it is concluded that the NTA molecules cannot effectively control the HAP crystal growth at temperature below 150 °C, leading to the formation of irregular microstructures in shape and nonhomogeneous in size. All the hydrothermal processes were carried out for 24 h, since during short time such as 16 and 20 h, no deposition was observed.

To investigate the effect of NTA concentration on HAP morphology, SEM images of the samples fabricated by various NTA:Ca molar ratios (0:1, 0.5:1, 1:1, 2:1, and 4:1) before and after heating are presented in Fig. 3a–e and Fig. 3f–j, respectively. A comparison of these images reveals that the morphology of HAP was strongly influenced by the NTA:Ca molar ratio. The morphology of HAP prepared at 180 °C for 24 h without using NTA (control test) consists of aggregated micro/nanorods with no regularity in dimensions and shapes.

When the chelating agent with an NTA:Ca molar ratio of 0.5:1 is added into the reaction, the dimensions of rod-like shapes distinctly decrease compared to the control test, concluding the ability of NTA to limit crystal growth. SEM images of the HAP generated with NTA:Ca molar ratio of 1:1, self-assembly of the rod-like shapes leads to form regular hierarchical microparticles in size ranging from 2 to 3 μm. More increase of NTA:Ca molar ratio from 1:1 to 2:1 and 4:1 show that the NTA molecules in high concentration can only decrease the crystal growth and size of HAP rods without regular assembly compared to the control test. Moreover, high aggregation of the rod-like particles makes difficult to estimate the dimensions of the rods.

To validate the formation of HAP and determine its crystal phase, the

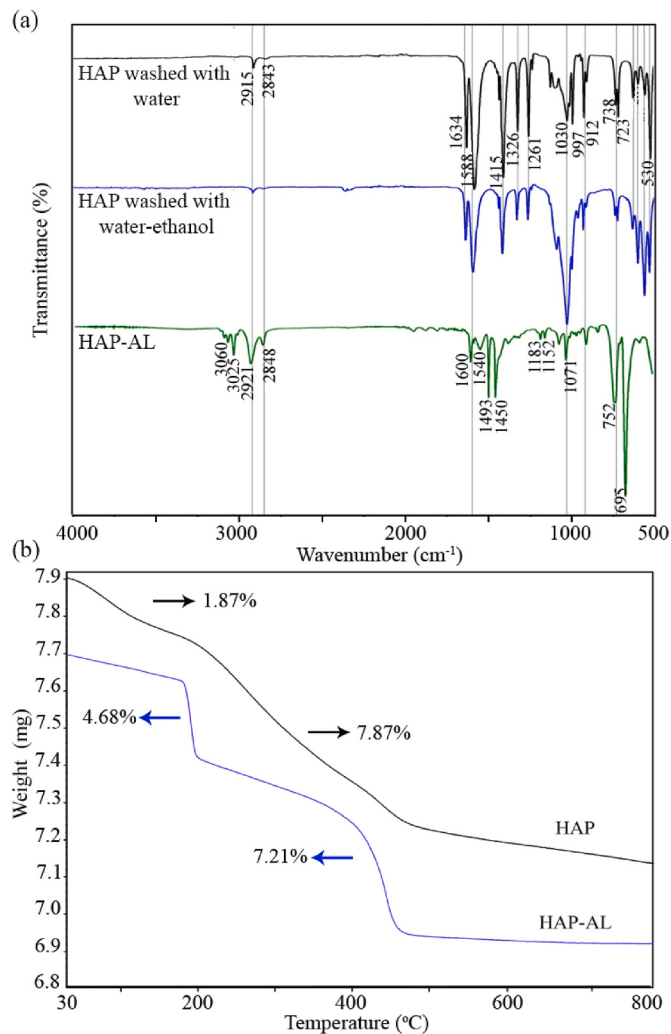


Fig. 6. (a) ATR spectra of HAP (sample S4T) peeled by PVA washed with water, water/ethanol (50% v/v), and water/ethanol (50% v/v) along with AL-functionalized (HAP-AL). (b) TGA curves of HAP (sample S4T) peeled by PVA washed with water/ethanol (50% v/v) and water/ethanol (50% v/v) along with AL-functionalized (HAP-AL).

samples were characterized using XRD and ATR techniques. Fig. 4a shows the XRD patterns of the samples S2–S4 and S2T–S4T. The diffraction peaks of crystals grown hydrothermally in the temperature range of 150–180 °C correspond to the hexagonal crystalline structure of HAP with the space group $P6_3/m$ (JCPDS No. 96–900–1234). Although the XRD patterns of the samples prepared at 150, 165, and 180 °C display the three main diffraction peaks of HAP around 31.9° (211), 32.4° (112), and 32.9° (300), the XRD pattern of the sample synthesized at 180 °C includes sharper and separated peaks in these range, indicating the high crystallinity of HAP formed at 180 °C. Besides the peaks related to the crystalline structure of HAP, the diffraction peaks located at 12.89° (001), 17.76° (110), (26.24°) (002), 26.76° (200) and 29.33° (120) attributed to the dicalcium phosphate hydrate (DCPH; JCPDS No. 01–070–1425) disappeared completely after thermal treatment, and pure mono-phase HAP could be obtained. Similar results were observed by Alge et al. [45] after thermal treatment at 400 °C. The formation percentage of DCPH phase of the samples prepared at 150, 165, and 180 °C estimated by Rietveld method [46] based on the peak located at 29.33° is 25%, 23% and 12%, respectively, indicating DCPH phase was transformed into HAP by increasing the hydrothermal temperature.

The ATR spectra of the as-deposited samples (S2–S4) before and after thermal treatment at 400 °C (S2T–S4T) are presented in Fig. 4b. The

Table 3

Distinct IR vibrations of the peeled HAP with PVA and AL-functionalized HAP.

Wavenumber (cm^{-1}) PVA-peeled HAP	Corresponding vibrations	Wavenumber (cm^{-1}) HAP-AL	Corresponding vibrations
2915	$\nu(\text{CH}_2)$; asymmetric stretching	3000–3200	$\nu(\text{OH and NH}_2)$; stretching
2843	$\nu(\text{CH}_2)$; symmetric stretching	2920	$\nu(\text{CH}_2)$; asymmetric stretching
1588	C=O stretching	2853	$\nu(\text{CH}_2)$; symmetric stretching
1415	C–H bending of CH_2	1600	(OH and NH_2) ; bending
1326	C–H bending of CH_3	1540	$\nu(\text{CH}_2)$; bending
1261	C–O stretching (v_1) of PO_4^{3-} ; asymmetric stretching	1493	$\nu(\text{CH}_2)$; stretching
1030	$\nu(\text{CH}_2)$; asymmetric stretching	1450	C–H bending
997	C–O stretching (v_3) of PO_4^{3-} ; symmetric stretching	1183	C–O stretching
930	- $(\text{CH}_2)_n$ bending	1152	C–O stretching
723	(v_1) of PO_4^{3-} ; asymmetric stretching	1071	(v_1) of PO_4^{3-} ; asymmetric stretching
632	(v_2) of PO_4^{3-} ; symmetric stretching	912	(v_3) of PO_4^{3-} ; symmetric stretching
562	(v_4) of PO_4^{3-} ; bending	752	(v_2) of PO_4^{3-} ; bending vibrations
530	C–H bending	695	(v_4) of PO_4^{3-} ; bending vibrations

adsorption bands around 670 – 680 cm^{-1} are attributed to the bending vibrations (v_4) of PO_4^{3-} , while bands centered at around 900 – 1100 cm^{-1} derive from the symmetric and asymmetric stretching vibrations (v_1 and v_3) of PO_4^{3-} [47]. These observations confirm the formation of HAP. The broad band at 3400 – 3600 cm^{-1} (stretching vibration of hydroxyl) and the band at around 1630 cm^{-1} (bending vibration of hydroxyl) in the as-prepared HAP are attributed to the crystal and surface adsorbed water molecules [48].

By considering the SEM images, we can propose growth mechanism of HAP hierarchical microparticles in the presence of NTA. When NTA as a tripodal tetridentate ligand is added into the aqueous solution of CaCl_2 , $[\text{Ca}(\text{NTA})]^-$ complex forms at the early stages of the reaction due to high tendency of amine and carboxylate groups of NTA to coordinate Ca^{2+} ions. Under hydrothermal pressure and temperature (150 – 180 °C), the cleavage of the Ca–NTA bounds occurs, Ca^{2+} ions gradually release to coordinate PO_4^{3-} ions, and HAP nuclei form. In other words, the $[\text{Ca}(\text{NTA})]^-$ complex can consider as a new precursor for the nucleation process in the solution. The as-formed HAP nuclei can be capped by the free NTA molecules, causing the limitation of particle growth in two directions, and forming one-dimensional (1-D) structures similar rod-like shapes. Finally, self-assembly of the rod-like shapes during 24 h leads to the formation of hierarchical microparticles. Fabrication of hierarchical shapes of HAP consisted of 1-D structures is the main structure formed in the presence of organic additives including carboxylate groups due to their chelating ability with Ca^{2+} ions [15,49].

To functionalize the HAP, peeling of the layer deposited on FTO was considered. For this purpose, the sample prepared at 180 °C with NTA/Ca molar ratio of 1:1 after thermal treatment was selected because of its high crystallinity and homogenous morphology than the layers deposited in other conditions. The peeling process was carried out using two different water-soluble polymers, Fluoromount™ and PVA. To consider morphological changes after peeling, FE-SEM images of the HAP powders obtained after peeling were provided and presented in Fig. 5. As we can see in Fig. 5a and b, the hierarchical microparticles show high

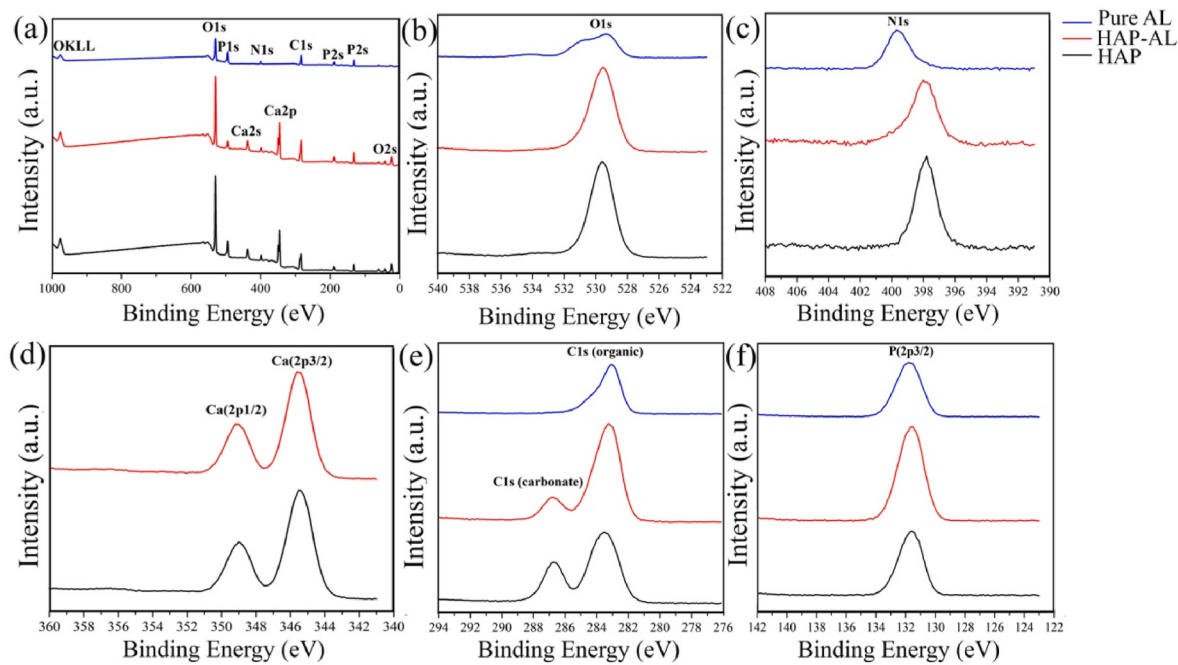


Fig. 7. XPS survey spectrum (a) and high-resolution XPS spectra of O1s (b), N1s (c), Ca2p (d), C1s (e), and P2p (f) of the HAP (sample S4T), HAP-AL and pure AL.

Table 4
Binding energies (eV) and their assignments of the HAP (S4T), HAP-AL and pure AL based on the XPS results.

Peak	HAP	HAP-AL	Pure AL	Ref.
O1s	529.6	529.6	529.3, 530.8	[57]
N1s	398.0	398.0	399.6	[58]
Ca2p _{1/2}	349.1	349.1	—	[59]
Ca2p _{3/2}	345.5	345.5	—	[59]
C1s (organic)	283.6	283.3	283.1	[57]
C1s (carbonate)	286.7	286.8	—	
P2p _{3/2}	131.7	131.6	131.8	[59]

aggregation after peeling by Fluoromount™ and the microparticles were fully covered by the reagent even after extra washing with water and ethanol. Fig. 5c and d displays FE-SEM images of the same microparticles peeled by PVA, which they are monodispersed particles with no obvious changes in morphology. This observation helping us to select PVA as suitable reagent to separate HAP layer from FTO substrate. In order to remove PVA after peeling, the HAP powders were purified by extra washing with water and a mixture of water plus ethanol (50% v/v). The ATR spectra of the peeled microparticles after washing with water and a mixture of water/ethanol (Fig. 6) show that the intensity of the peaks located around 2915 (ν (CH₂) asym), 2843 (ν (CH₂) sym), 1588 (C=O stretching), 1415 (C-H bending of CH₂), 1326 (OH rocking with CH wagging), 1261 (C-O stretching), 997 (C-O stretching), 723 ((CH₂)_n bending) and 530 cm⁻¹ (C-H bending) attributed to PVA structure [50,51] decreased after washing by water/ethanol, while the corresponding vibrations of the PO₄³⁻ group at 1030, 930, 632 and 562 cm⁻¹ increased, indicating the removal of almost all of PVA with a mixture of water/ethanol.

After peeling the HAP layer, surface of the hierarchical microspheres was modified by AL molecules. Based on the available studies, it was demonstrated that AL shows more affinity for calcium phosphate crystals compared to other bisphosphonates due to its structure including one hydroxyl group and two phosphate groups bound to the central carbon, enhancing its tendency to HAP via tridentate binding to calcium [39,52]. In this work, microspheres of HAP were treated with aqueous solution of AL at room temperature for 24 h. Quan and co-workers [53]

have observed that surface modification of HAP nanocrystals with high concentration of AL (8 mM) shows higher bioactivity rather than lower concentrations. Therefore, the peeled hierarchical microspheres of HAP were treated with 8 mM aqueous solution of AL. FE-SEM images of the AL-treated HAP displayed in Fig. 5e and f revealed that surface-modified microparticles with AL has no morphological changes compared to the peeled particles (Fig. 5c and d). Nevertheless, it is necessary to study chemical composition of HAP surface after functionalization. Thereby, ATR spectrum of the AL-functionalized HAP was recorded and presented in Fig. 6a. It is clear the appearance of new peaks around 3025–3060 (OH and NH₂ stretching), 2921–2848 (CH₂ stretching), 1600 (OH and NH₂ bending), 1540 (CH₂ bending), 1493 (CH₂ stretching), 1450 (C–H bending), 1183–1152 (C–O stretching), 912 (ν_3), 752 (ν_2), and 695 cm⁻¹ (ν_4) of PO₄³⁻ assigned to the AL structure [54,55]. To brief study, the main vibrations have been summarized in Table 3. In addition, the peak corresponding to the PO₄³⁻ groups shows significant shift from 1030 cm⁻¹–1071 cm⁻¹, indicating chemical binding of PO₄³⁻ groups of AL and Ca²⁺ sites in crystal structure of HAP. As a result, ATR spectroscopy authenticated surface modification of HAP with AL molecules including –NH₂ groups as an effective linker. To obtain a detailed description of thermal behavior of the HAP microparticles (S4T) before and after functionalization, TGA curves of the samples were recorded (Fig. 6b). TGA curve of the HAP microparticles displays two distinct slope changes at 30–480 °C including weight loss of 1.87% and 7.87%, in which progressively water is losing. A continuous mass loss corresponding to the dehydroxylation of HAP with the release of water and formation of oxyhydroxyapatite at temperature above 480 °C can be observed [56]. TGA curve of the sample S4T obtained after AL treatment shows two clear weight loss steps between 30 and 220 °C (4.68%) and 220–470 °C (7.21%). The removal of water and the ammonia from AL molecules in the first step (4.68%) and pyrolysis of organic compound in the second step (7.21%) take place. The outstanding weight loss in the first step of the functionalized HAP confirms the binding of AL molecules to the HAP microparticles.

It is predicted that physical and chemical properties of HAP surface after functionalization can be varied. To consider the surface area and its chemical composition, BET and XPS techniques have been used. Based on the BET results, the specific surface area of the as-prepared and functionalized HAP is 94 m²g⁻¹ and 34 m²g⁻¹, respectively. The

reduction of the specific surface area approves the binning of AL molecules onto the HAP surface. Fig. 7a–c shows the XPS survey and high resolution spectra of the as-prepared HAP (S4T), AL-functionalized HAP and pure AL. The binding energy values and their assignments have been also summarized in Table 4. The survey spectrum (Fig. 7a) consists of the characterized peaks related to Ca, P, N, O and C elements for the HAP and HAP-AL samples. Detection of N and C elements for the HAP is due to the NTA residue. Fig. 7b displays that the binding energy of the O1s and P1s peaks located at 529.3 and 494.8 eV, respectively, without no changes for pure AL, HAP-AL and the as-prepared HAP. As shown in Fig. 7c, the binding energy of the Ca2p (345.4 and 349.1 eV) and C1s (283.5 and 286.7 eV) has no shift for pure AL, HAP-AL and HAP. The C1s peaks at 283.5 and 286.7 eV for HAP can be concluded of the NTA residue and surface carbonate adsorbed from air [57]. More consideration reveals that the P2p peak was shifted from 131.8 (pure AL) to 131.6 eV (HAP-AL). Besides, the N1s peak of the HAP-AL appeared at 398.0 eV that was shifted to the lower binding energy compared to the pure AL (399.6 eV). The binding energies shifted to the lower energies are consequences of the chemical binding of the phosphate and amine groups of AL to the HAP microparticles. This evidence asserts the previous results obtained from the ATR-FTIR spectra about the functionalization of HAP with AL molecules.

4. Conclusions

This work demonstrates that using calcium and phosphate precursors in a Ca/P molar ratio of 1.67:1 via hydrothermal approach is a suitable method to prepare HAP on FTO. For the first time, tetradeятate NTA chelating agent was used to control the crystal growth of HAP. The effect of different concentrations of NTA on HAP fabrication was studied, and the results revealed the successful formation of hierarchical microparticles when the NTA/Ca molar ratio is equimolecular. The effect of hydrothermal temperature varied from 120 to 180 °C on HAP formation was also investigated, and the obtained results showed that high-crystalline hierarchical structures of HAP with particle sizes between 2.5 and 3.5 μm were obtained at 180 °C for 24 h using NTA in a NTA/Ca molar ratio of 1:1. Comparing this work with prior studies on the hydrothermal deposition of HAP on metal substrates in the presence of carboxylate compounds such as EDTA and potassium sodium tartrate at 200 °C for 24 h, this work presents near energy consumption to fabricate crystalline HAP. To functionalize the as-prepared HAP, the layer grown on FTO was peeled using Fluoromount™ and PVA. The HAP layer peeled with PVA showed no distinct morphological changes, maintaining the hierarchical structures. The HAP powders obtained after PVA peeling were functionalized by AL molecules. The chemical shift of PO₄³⁻ peaks observed by ATR-FTIR and XPS spectroscopy, and reduced specific surface area after functionalization confirmed the functionalized of HAP. As a results, NTA-assisted synthesis and functionalization of hierarchical HAP structures with AL can be considered in medical applications due to the design of potential multifunctional biomaterials.

Declaration of competing interest

The authors declare that they have no known competing financial interests or personal relationships that could have appeared to influence the work reported in this paper.

Acknowledgments

The authors acknowledge Grant PID2020-115663 GB-C32 funded by MCIN/AEI/10.13039/501100011033, and the CCiT-UB for the use of their equipment. The authors also acknowledge the contribution of Dr. Lluïssa Pérez-García and Dr. Albert Gutierrez Currius for laboratory services. Fatemeh Mohandes thanks the European Research Council, and the Spanish Ministry for Science and Innovation for granting of María Zambrano postdoctoral fellowship (UNI/551/2021).

References

- [1] L.L. Hench, J.M. Polak, Third-generation biomedical materials, *Science* 295 (5557) (2002) 1014–1017, <https://doi.org/10.1126/science.1067404>.
- [2] C. Ning, L. Zhou, G. Tan, Fourth-generation biomedical materials, *Mater. Today Off. Off.* 19 (1) (2016) 2–3, <https://doi.org/10.1016/j.mattod.2015.11.005>.
- [3] S.J. Park, M.M. Rahman, J. Lee, S.W. Kang, S. Kim, Investigation of bone regeneration efficacy of new bovine bone minerals in a canine mandibular critical defect model, *Adv. Healthcare Mater.* (2023) e2202942, <https://doi.org/10.1002/adhm.202202942>.
- [4] S. Bhat, U. Uthappa, T. Altalhi, H.-Y. Jung, M.D. Kurkuri, Functionalized porous hydroxyapatite scaffolds for tissue engineering applications: a focused review, *ACS Biomater. Sci. Eng.* 8 (10) (2021) 4039–4076, <https://doi.org/10.1021/acsbiomaterials.1c00438>.
- [5] T. Gomathi, P. Sudha, S. Thomas, *Nanobiomaterials: Research Trends and Applications*, first ed., CRC Press, 2023, pp. 30–32.
- [6] V.A. Dubok, Bioceramics—yesterday, today, tomorrow, *Powder Metall. Met. Ceram.* 39 (2000) 381–394, <https://doi.org/10.1023/A:1026617607548>.
- [7] K.S. Naik, *Advanced bioceramics*, in: *Advances in Biological Science Research*, Elsevier, 2019, pp. 411–417.
- [8] S. Koutsopoulos, Synthesis and characterization of hydroxyapatite crystals: a review study on the analytical methods, *J. Biomed. Mater. Res.* 62 (4) (2002) 600–612, <https://doi.org/10.1002/jbm.10280>.
- [9] J.A. Lett, M. Sundareswari, K. Ravichandran, M.B. Latha, S. Sagadevan, M.R. B. Johan, Tailoring the morphological features of sol-gel synthesized mesoporous hydroxyapatite using fatty acids as an organic modifier, *RSC Adv.* 9 (11) (2019) 6228–6240, <https://doi.org/10.1039/C9RA00051H>.
- [10] F. Mohandes, M. Salavati-Niasari, Simple morphology-controlled fabrication of hydroxyapatite nanostructures with the aid of new organic modifiers, *Chem. Eng. J.* 252 (2014) 173–184, <https://doi.org/10.1016/j.cej.2014.05.026>.
- [11] D.J. Haders, A. Burukhin, E. Zlotnikov, R.E. Rimau, TEP/EDTA doubly regulated hydrothermal crystallization of hydroxyapatite films on metal substrates, *Chem. Mater.* 20 (22) (2008) 7177–7187, <https://doi.org/10.1021/cm071628c>.
- [12] M.-G. Ma, Hierarchically nanostructured hydroxyapatite: hydrothermal synthesis, morphology control, growth mechanism, and biological activity, *Int. J. Nanomed.* (2012) 1781–1791, <https://doi.org/10.2147/IJN.S29884>.
- [13] S.H. Rhee, J. Tanaka, Hydroxyapatite coating on a collagen membrane by a biomimetic method, *J. Am. Ceram. Soc.* 81 (11) (1998) 3029–3031, <https://doi.org/10.1111/j.1151-2916.1998.tb02734.x>.
- [14] M. Sadat-Shojaei, M.-T. Khorasani, E. Dinpanah-Khoshdargi, A. Jamshidi, Synthesis methods for nanosized hydroxyapatite with diverse structures, *Acta Biomater.* 9 (8) (2013) 7591–7621, <https://doi.org/10.1016/j.actbio.2013.04.012>.
- [15] Y. In, U. Amornkitbamrung, M.-H. Hong, H. Shin, On the crystallization of hydroxyapatite under hydrothermal conditions: role of sebacic acid as an additive, *ACS Omega* 5 (42) (2020) 27204–27210, <https://doi.org/10.1021/acsomega.0c03297>.
- [16] A. Lak, M. Mazloumi, M. Mohajerani, A. Kajbafvala, S. Zanganeh, H. Arami, S. Sadrnezhaad, Self-assembly of dandelion-like hydroxyapatite nanostructures via hydrothermal method, *J. Am. Ceram. Soc.* 91 (10) (2008) 3292–3297, <https://doi.org/10.1111/j.1551-2916.2008.02600.x>.
- [17] G. Singh, S.S. Jolly, R.P. Singh, Investigation of surfactant role in synthesis of hydroxyapatite nanorods under microwave and hydrothermal conditions, *Mater. Today: Proc.* 26 (2020) 2701–2710, <https://doi.org/10.1016/j.matpr.2020.02.568>.
- [18] C. Xue, Y. Chen, Y. Huang, P. Zhu, Hydrothermal synthesis and biocompatibility study of highly crystalline carbonated hydroxyapatite nanorods, *Nanoscale Res. Lett.* 10 (2015) 1–6, <https://doi.org/10.1186/s11671-015-1018-9>.
- [19] X. Xu, X. Sun, Y. Tian, L. Zhang, L. Liu, Osteogenic activity of a micro/nano hierarchical nano-hydroxyapatite coating on zirconium alloy, *Mater. Char.* 205 (2023) 113356, <https://doi.org/10.1016/j.matchar.2023.113356>.
- [20] H. Zhang, C. Zhang, S.-D. Jiang, Morphology evolution of Hydroxyapatite: synergistic effects and water treatment application, *Mater. Lett.* 341 (2023) 134288, <https://doi.org/10.1016/j.matlet.2023.134288>.
- [21] D. Xu, Y. Wan, Z. Xie, C. Du, Y. Wang, Hierarchically structured hydroxyapatite particles facilitate the enhanced integration and selective anti-tumor effects of amphiphilic prodrug for osteosarcoma therapy, *Adv. Healthcare Mater.* (2023) 2202668, <https://doi.org/10.1002/adhm.202202668>.
- [22] H.A. Mottola, Nitrilotriacetic acid as a chelating agent: applications, toxicology, and bio-environmental impact, *Toxicol. Environ. Chem.* 2 (2) (1974) 99–161, <https://doi.org/10.1080/02772247409356922>.
- [23] D. Wu, X. Xie, Y. Ma, J. Zhang, C. Hou, X. Sun, X. Yang, Y. Zhang, H. Kimura, W. Du, Morphology controlled hierarchical NiS/carbon hexahedrons derived from nitrilotriacetic acid-assembly strategy for high-performance hybrid supercapacitors, *Chem. Eng. J.* 433 (2022) 133673, <https://doi.org/10.1016/j.cej.2021.133673>.
- [24] Z. Xiao, J. Zhang, Y. Xia, L. Zhu, L. Lei, S. Xu, Nanoplates-assembled Bi₂WO₆ microcoins with hierarchical porous structure as efficient visible-light-active photocatalysts, *Mater. Res. Bull.* 94 (2017) 322–327, <https://doi.org/10.1016/j.materresbull.2017.06.013>.
- [25] J. Zhao, X. Yu, Z. Gao, W. Zhao, R. Xu, Y. Liu, H. Shen, One step synthesis of SnS₂ nanosheets assembled hierarchical tubular structures using metal chelate nanowires as a soluble template for improved Na-ion storage, *Chem. Eng. J.* 332 (2018) 548–555, <https://doi.org/10.1016/j.cej.2017.09.110>.
- [26] M.H. Abdelazim, A.H. Abdelazim, W.F. Ismaiel, M.E. Alsobky, A. Younes, A. M. Hadeya, S. Ramzy, M. Shahin, Effect of intra-nasal nitrilotriacetic acid trisodium salt in lowering elevated calcium cations and improving olfactory

- dysfunction in COVID-19 patients, *Eur. Arch. Oto-Rhino-Laryngol.* 279 (9) (2022) 4623–4628, <https://doi.org/10.1007/s00405-022-07424-5>.
- [27] T.T. Paterlini, L.F. Nogueira, C.B. Tovani, M.A. Cruz, R. Derradi, A.P. Ramos, The role played by modified bioinspired surfaces in interfacial properties of biomaterials, *Biophys. Rev.* 9 (5) (2017) 683–698, <https://doi.org/10.1007/s12551-017-0306-2>.
- [28] L. Chen, J.M. McCrate, J.C. Lee, H. Li, The role of surface charge on the uptake and biocompatibility of hydroxyapatite nanoparticles with osteoblast cells, *Nanotechnology* 22 (10) (2011) 105708, <https://doi.org/10.1088/0957-4484/22/10/105708>.
- [29] L. Memè, A. Santarelli, G. Marzo, M. Emanuelli, P. Nocini, D. Bertossi, A. Putignano, M. Dioguardi, L.L. Muzio, F. Bambini, Novel hydroxyapatite biomaterial covalently linked to raloxifene, *Int. J. Immunopathol. Pharmacol.* 27 (3) (2014) 437–444, <https://doi.org/10.1177/039463201402700315>.
- [30] B. Palazzo, M. Iafisco, M. Laforgia, N. Margiotta, G. Natile, C.L. Bianchi, D. Walsh, S. Mann, N. Roveri, Biomimetic hydroxyapatite-drug nanocrystals as potential bone substitutes with antitumor drug delivery properties, *Adv. Funct. Mater.* 17 (13) (2007) 2180–2188, <https://doi.org/10.1002/adfm.200600361>.
- [31] G. Wang, Z. Lv, T. Wang, T. Hu, Y. Bian, Y. Yang, R. Liang, C. Tan, X. Weng, Surface functionalization of hydroxyapatite scaffolds with MgAlEu-LDH nanosheets for high-performance bone regeneration, *Adv. Sci.* 10 (1) (2023) 2204234, <https://doi.org/10.1002/advs.202204234>.
- [32] M.P. Whyte, W.H. McAlister, V. Dhiman, N.R. Gopinathan, S.K. Bhadada, Drug-induced osteoporosis, *Bone* 173 (2023) 116788, <https://doi.org/10.1016/j.bone.2023.116788>.
- [33] G.P. Keeling, F. Baark, O.L. Katsamenis, J. Xue, P.J. Blower, S. Bertazzo, R. Tm de Rosales, ^{68}Ga -bisphosphonates for the imaging of extraosseous calcification by positron emission tomography, *Sci. Rep.* 13 (1) (2023) 14611, <https://doi.org/10.1038/s41598-023-41149-7>.
- [34] S.I. Mostafa, M.S. Ismail, H.A. Mohammed, M.F. Osman, N.A. Elwassefy, Magnetic hydroxyapatite bisphosphonate-based composites: a bone-targeting nanosystem, *Emerg. Mater.* 6 (4) (2023) 1273–1284, <https://doi.org/10.1007/s42247-022-00430-7>.
- [35] K.K. Lee, N. Raja, H.-s. Yun, S.C. Lee, C.-S. Lee, Multifunctional bone substitute using carbon dot and 3D printed calcium-deficient hydroxyapatite scaffolds for osteoclast inhibition and fluorescence imaging, *Acta Biomater.* 159 (2023) 382–393, <https://doi.org/10.1016/j.actbio.2023.01.028>.
- [36] R.A. Nadar, N. Margiotta, M. Iafisco, J.J. van den Beucken, O.C. Boerman, S. C. Leeuwenburgh, Bisphosphonate-functionalized imaging agents, anti-tumor agents and nanocarriers for treatment of bone cancer, *Adv. Healthcare Mater.* 6 (8) (2017) 1601119, <https://doi.org/10.1002/adhm.201601119>.
- [37] D. Li, Y. Zhu, Z. Liang, Alendronate functionalized mesoporous hydroxyapatite nanoparticles for drug delivery, *Mater. Res. Bull.* 48 (6) (2013) 2201–2204, <https://doi.org/10.1016/j.materresbull.2013.02.049>.
- [38] E. Boanini, P. Torricelli, M. Gazzano, R. Giardino, A. Bigi, Alendronate-hydroxyapatite nanocomposites and their interaction with osteoclasts and osteoblast-like cells, *Biomater* 29 (7) (2008) 790–796, <https://doi.org/10.1016/j.biomaterials.2007.10.040>.
- [39] M.-H. Ri, Y.-M. Jang, U.-S. Ri, C.-J. Yu, K.-I. Kim, S.-U. Kim, Ab initio investigation of adsorption characteristics of bisphosphonates on hydroxyapatite (001) surface, *J. Mater. Sci.* 53 (6) (2018) 4252–4261, <https://doi.org/10.1007/s10853-017-1880-1>.
- [40] J. Klara, J. Lewandowska-Laćucka, How efficient are alendronate-nano/biomaterial combinations for anti-osteoporosis therapy? An evidence-based review of the literature, *Int. J. Nanomed.* (2022) 6065–6094, [10.1021/IJN.S388430](https://doi.org/10.1021/IJN.S388430).
- [41] Y. Wang, Q. Huang, X. He, H. Chen, Y. Zou, Y. Li, K. Lin, X. Cai, J. Xiao, Q. Zhang, Multifunctional melanin-like nanoparticles for bone-targeted chemo-photothermal therapy of malignant bone tumors and osteolysis, *Biomater* 183 (2018) 10–19, <https://doi.org/10.1016/j.biomaterials.2018.08.033>.
- [42] P. Szterner, M. Biernat, The synthesis of hydroxyapatite by hydrothermal process with calcium lactate pentahydrate: the effect of reagent concentrations, pH, temperature, and pressure, *Bioinorgan. Chem. Appl.* 2022 (2022) 13, <https://doi.org/10.1155/2022/3481677>.
- [43] C. Li, X. Li, Q. Zhang, L. Li, S. Wang, The alkaline fusion-hydrothermal synthesis of hydroxyapatite-zeolite (HAP-ZE) from blast furnace slag (BFS): effects of reaction temperature, *Minerals* 11 (11) (2021) 1160, <https://doi.org/10.3390/min11111160>.
- [44] S. Lazić, S. Zec, N. Miljević, S. Milonjić, The effect of temperature on the properties of hydroxyapatite precipitated from calcium hydroxide and phosphoric acid, *Thermochim. Acta* 374 (1) (2001) 13–22, [https://doi.org/10.1016/S0040-6031\(01\)00045-1](https://doi.org/10.1016/S0040-6031(01)00045-1).
- [45] D.L. Alge, G. Santa Cruz, W.S. Goebel, T.-M.G. Chu, Characterization of dicalcium phosphate dihydrate cements prepared using a novel hydroxyapatite-based formulation, *Biomod. Mater.* 4 (2) (2009) 025016, <https://doi.org/10.1088/1748-6041/4/2/025016>.
- [46] D.L. Bish, S. Howard, Quantitative phase analysis using the Rietveld method, *J. Appl. Crystallogr.* 21 (2) (1988) 86–91, <https://doi.org/10.2451/2019PM870>.
- [47] J.S. Cho, S.-H. Rhee, Formation mechanism of nano-sized hydroxyapatite powders through spray pyrolysis of a calcium phosphate solution containing polyethylene glycol, *J. Eur. Ceram. Soc.* 33 (2) (2013) 233–241, <https://doi.org/10.1016/j.jeurceramsoc.2012.08.029>.
- [48] T. Seki, K.-Y. Chiang, C.-C. Yu, X. Yu, M. Okuno, J. Hunger, Y. Nagata, M. Bonn, The bending mode of water: a powerful probe for hydrogen bond structure of aqueous systems, *J. Phys. Chem. Lett.* 11 (19) (2020) 8459–8469, <https://doi.org/10.1021/acs.jpclett.0c01259>.
- [49] S.H. Daryan, A. Khavandi, J. Javadpour, Surface engineered hollow hydroxyapatite microspheres: hydrothermal synthesis and growth mechanisms, *Solid State Sci.* 106 (2020) 106301, <https://doi.org/10.1016/j.soliddstateciences.2020.106301>.
- [50] A.S. Asran, S. Henning, G.H. Michler, Polyvinyl alcohol–collagen–hydroxyapatite biocomposite nanofibrous scaffold: mimicking the key features of natural bone at the nanoscale level, *Polymer* 51 (4) (2010) 868–876, <https://doi.org/10.1016/j.polymer.2009.12.046>.
- [51] Y. Liu, L.M. Geever, J.E. Kennedy, C.L. Higginbotham, P.A. Cahill, G. B. McGuinness, Thermal behavior and mechanical properties of physically crosslinked PVA/Gelatin hydrogels, *J. Mech. Behav. Biomed. Mater.* 3 (2) (2010) 203–209, <https://doi.org/10.1016/j.jmbbm.2009.07.001>.
- [52] S. Anjum, D.K. Arya, M. Saeed, D. Ali, M.S. Athar, W. Yulin, S. Alarifi, X. Wu, P. Rajinikanth, Q. Ao, Multifunctional electrospun nanofibrous scaffold enriched with alendronate and hydroxyapatite for balancing osteogenic and osteoclast activity to promote bone regeneration, *Front. Bioeng. Biotechnol.* 11 (2023) 18, <https://doi.org/10.3389/fbioe.2023.1302594>.
- [53] H. Quan, Y. He, J. Sun, W. Yang, W. Luo, C. Dou, F. Kang, C. Zhao, J. He, X. Yang, Chemical self-assembly of multifunctional hydroxyapatite with a coral-like nanostructure for osteoporotic bone reconstruction, *ACS Appl. Mater. Interfaces* 10 (30) (2018) 25547–25560, <https://doi.org/10.1021/acsami.8b00987>.
- [54] S. Ibrahim, S. I Khalivulla, G.A. Akowuh, Determination of alendronate sodium in tablets by attenuated total reflectance Fourier transform infrared spectroscopy, *Curr. Bioact. Compd.* 13 (1) (2017) 71–77, <https://doi.org/10.2174/1573407212999160506112738>.
- [55] L. Ochiuz, C. Grigoras, M. Popa, I. Stoleriu, C. Munteanu, D. Timofte, L. Profire, A. G. Grigoras, Alendronate-loaded modified drug delivery lipid particles intended for improved oral and topical administration, *Molecules* 21 (7) (2016) 858, <https://doi.org/10.3390/molecules21070858>.
- [56] N.V. Bulina, S.V. Makarova, S.G. Baev, A.A. Matvienko, K.B. Gerasimov, O. A. Logutenko, V.S. Bystrov, A study of thermal stability of hydroxyapatite, *Minerals* 11 (12) (2021) 1310, <https://doi.org/10.3390/min11121310>.
- [57] G. Gomes, F. Borghi, R. Ospina, E. López, F. Borges, A. Mello, Nd: YAG (532 nm) pulsed laser deposition produces crystalline hydroxyapatite thin coatings at room temperature, *Surf. Coat. Technol.* 329 (2017) 174–183, <https://doi.org/10.1016/j.surfcoat.2017.09.008>.
- [58] Ž. Petrović, A. Šarić, I. Despotović, J. Katić, R. Peter, M. Petracović, M. Petković, A new insight into coating's formation mechanism between TiO₂ and alendronate on titanium dental implant, *Materials* 13 (14) (2020) 3220, <https://doi.org/10.3390/ma13143220>.
- [59] H.B. Lu, C.T. Campbell, D.J. Graham, B.D. Ratner, Surface characterization of hydroxyapatite and related calcium phosphates by XPS and TOF-SIMS, *Anal. Chem.* 72 (13) (2000) 2886–2894, <https://doi.org/10.1021/ac990812h>.